Geology, Geophysics & Environment 2025, vol. 51 (2): 173–191

Decomposition of displacement vectors from InSAR images of mining areas – a case study

Andrzej Kwinta[1], Anna Kopeć[2], Krystyna Michałowska[3]

[1] *University of Agriculture in Krakow, Faculty of Environmental Engineering and Surveying, Krakow, Poland, e-mail: andrzej.kwinta@urk.edu.pl (corresponding author), ORCID ID: 0000-0002-2003-7703*
[2] *Wrocław University of Science and Technology, Faculty of Geoengineering, Mining and Geology, Wrocław, Poland, e-mail: anna.kopec@pwr.edu.pl, ORCID ID: 0000-0002-5861-1280*
[3] *AGH University of Krakow, Faculty of Geo-Data Science, Geodesy, and Environmental Engineering, Krakow, Poland, e-mail: michalowska@agh.edu.pl, ORCID ID: 0000-0001-7749-3622*

Received: 10 January 2025; accepted: 6 June 2025; first published online: 20 July 2025

Abstract: Mining activities are a major anthropogenic driver of ground surface deformation, often resulting in complex subsidence phenomena that are difficult to characterize using conventional geodetic methods. Interferometric synthetic aperture radar (InSAR) provides a powerful means of detecting displacements over large areas, but decomposing its line-of-sight (LOS) measurements into full 3D displacement vectors remains a challenge, especially when limited to data from two satellite tracks. This paper presents an iterative decomposition algorithm that supplements the classical two-LOS system with an empirical relationship between horizontal displacement components and the slope of the subsidence trough, derived from established mining deformation theories. The algorithm is validated through both a theoretical "blind" test case and three real-life examples of mining-induced seismic deformation in the Legnica-Głogów Copper District (LGCD), Poland. The results show that the proposed method significantly improves the accuracy of displacement vector estimation compared to classical decomposition techniques. This approach not only enhances our understanding of mining-induced ground movements but also offers practical benefits for ground surface deformation monitoring and hazard assessment in subsidence-prone regions.

Keywords: InSAR, mining tremors; mining deformations

INTRODUCTION

Societal development is closely entwined with technological advances which are fuelled by the consumption of minerals. Underground mining degrades all natural environment components (Kratzsch 1983, Blachowski et al. 2014). Researchers have studied the adverse direct, indirect, and secondary impacts of mining on the environment for years (Kratzsch 1983, Peng 1986, Chugh et al. 1989, Yan et al. 2016). Direct impact involves displacement and deformation of the rock mass and ground surface caused by the movement of rock towards the mine void. Indirect impact includes associated phenomena such as groundwater drawdown (Loupasakis 2014). Secondary effects can be linked to displacement caused by mining-induced tremors (Shen et al. 2008). Hence, the post-mining deformation process is a cause-and-effect problem. Its root cause is the extraction of a certain volume (continuity disturbance), leading to the displacement of the rock mass and ground surface ('towards' the mine void) (Kwinta 2003, Tajduś 2015). Mining operations are not the only anthropogenic cause of extensive ground surface displacement (Galloway & Burbey 2011, Camós

https://doi.org/10.7494/geol.2025.51.2.173 ISSN 2299-8004 | e-ISSN 2353-0790 | Wydawnictwa AGH

& Molins 2015, Pasquali et al. 2015, Castelazzi et al. 2016, Wang et al. 2019, Cigna & Tapete 2022, Karizmadeh et al. 2022, Yang et al. 2023)

Ground subsidence troughs were first recorded using surveying methods in the nineteenth century. Since experts could measure vertical and horizontal displacements, they have searched for a relationship between these values (Niemczyk 1935, Avershin 1946). Various researchers tried to reach general conclusions about the problem from individual observations (cases) of ground surface displacement. The application of Global Navigation Satellite Systems (GNSS) surveying techniques empowers scientists to monitor mining-induced terrain deformations with even greater detail (Hejmanowski & Kwinta 1997, 2001, Zhao et al. 2013). Furthermore, since the last decade of the 20th century, InSAR is of particular value in this case (Perski 1998, Ge et al. 2007, Blachowski et al. 2018). The ability of InSAR to cover large areas without the need for ground-based infrastructure offers a distinct advantage in complex mining environments. Furthermore, InSAR techniques allow for long-term monitoring and can help distinguish between different sources of ground motion, including subsidence caused by the direct influence of mining operations (Witkowski et al. 2021, Xie et al. 2024) and also mining-induced tremors (Malinowska et al. 2018, Milczarek et al. 2021).

Regrettably, the limitations of sensor technology and sensor positioning relative to the surface lead to problems with decomposing measured displacement vectors into three displacement vectors along the axes of the coordinate system. Assuming two radar images are used from satellites on different polar orbits (ascending and descending), they yield exactly two displacement vector components (Chang et al. 2017, Dong et al. 2021, Dittrich et al. 2022). When synthetic aperture radar (SAR) image data are collected from a single satellite, only a specific imaging direction can be discussed. When images come from two satellites, and their LOS vectors are not collinear, it is possible to obtain two axial components directly without the third component (third satellite data). In addition, due to the circumpolar orbits of SAR satellites, they are insensitive to the N–S component of horizontal displacement (Wright et al. 2004).

In this study, a solution for decomposing LOS vectors from differential interferometric SAR (DInSAR) measurements into three components of displacement field vectors was tested. A mathematical description of the displacement field in 3D and the resulting computational effects is presented. Issues of insufficient information to determine all three components of the LOS vector based on SAR images with different geometries is resolved, through the observed proportionality of mining deformation indicators (Niemczyk 1935, Avershin 1947, Litwiniszyn 1974) resulting from analyses of survey results and model research. Considerations on this topic can also be found in other publications (Wang et al. 2020, Yang et al. 2020).

It is a daunting challenge to pursue analyses in mining areas because of the complexity of how impacts are observable and the interference of diverse deformation phenomena (direct, indirect, and secondary impacts). What makes such analyses even more strenuous is that the mining and geological environment is often complicated (Hejmanowski & Kwinta 2010). For this reason, the problem of LOS vector decomposition for a displacement field induced by the extraction of a single seam of copper ore in Poland (LGCD) was investigated. The analyses involved short-term tremor-induced deformations to limit the influence of additional deformations. If the decomposition procedure proves successful, it can be enhanced to cover more complex cases. The preliminary analysis of the proposed solution will first involve a theoretical (blind) case. It will then be applied to three real-life case scenarios.

DInSAR LOS VECTORS

The coordinate system for the analyses and the coordinates of the vectors within this system are first defined. The computations are performed in a right-handed, three-dimensional Cartesian coordinate system. The axes (x, y, z) and the rotation directions (θ_x, θ_y, θ_z) are assumed as shown in Figure 1.

Axial rotations in the 3D system are considered. The problem of coordinate system conversion based on a combination of rotations can be addressed using Euler angles. Three elemental rotations to the right are applied.

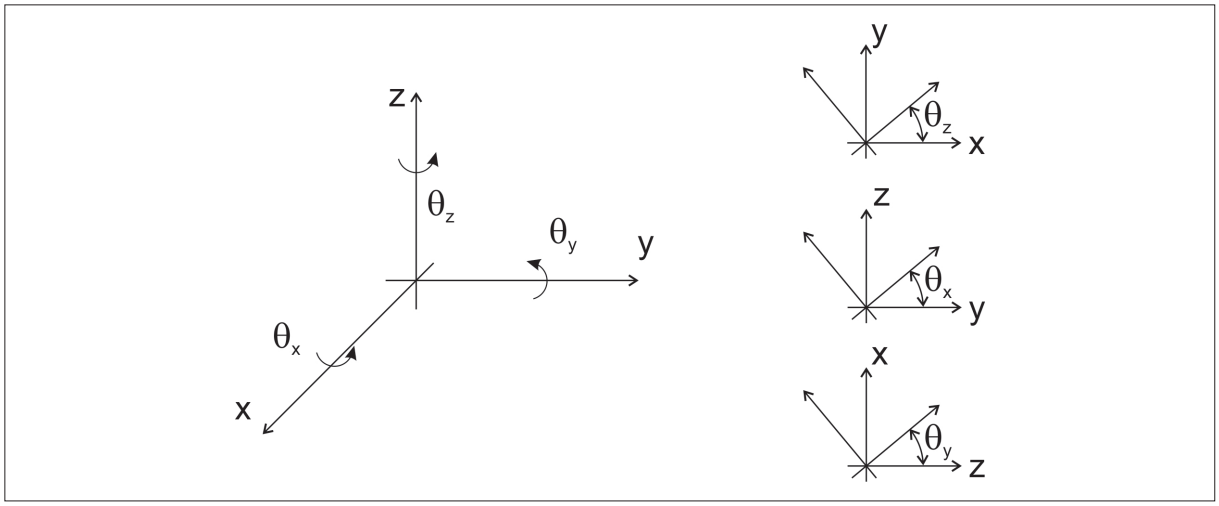

Fig. 1. *Three-dimensional coordinate system*

Assuming labels as in Figure 1:

– Matrix $\mathbf{R}_x$ of rotation about the *x*-axis (angle in the *yz* plane)

$$\mathbf{R}_x = \begin{bmatrix} 1 & 0 & 0 \\ 0 & \cos\theta_x & \sin\theta_x \\ 0 & -\sin\theta_x & \cos\theta_x \end{bmatrix} \tag{1}$$

– Matrix $\mathbf{R}_y$ of rotation about the *y*-axis (angle in the *xz* plane)

$$\mathbf{R}_y = \begin{bmatrix} \cos\theta_y & 0 & -\sin\theta_y \\ 0 & 1 & 0 \\ \sin\theta_y & 0 & \cos\theta_y \end{bmatrix} \tag{2}$$

– Matrix $\mathbf{R}_z$ of rotation about the *z*-axis (angle in the *xy* plane)

$$\mathbf{R}_z = \begin{bmatrix} \cos\theta_z & \sin\theta_z & 0 \\ -\sin\theta_z & \cos\theta_z & 0 \\ 0 & 0 & 1 \end{bmatrix} \tag{3}$$

Any rotation matrix $\mathbf{R}$ is a composition of three elemental rotations

$$\mathbf{R} = \mathbf{R}_z \cdot \mathbf{R}_y \cdot \mathbf{R}_x \tag{4}$$

Hence, considering Equations (1)–(4) and minding the order of rotations:

$$\mathbf{R} = \begin{bmatrix} B_x B_y B_z - A_x A_z & B_x B_y A_z + A_x B_z & -B_X A_y \\ -A_x B_y B_z - B_x A_z & -A_x B_y A_z + B_x B_z & A_x A_y \\ A_y B_z & A_y A_z & B_y \end{bmatrix} \tag{5}$$

where $A_i = \sin\theta_i$ and $B_i = \cos\theta_i$.

If the three components of any displacement vector $\mathbf{u}_0$ in a given coordinate system (*x*, *y*, *z*) are known, it can be transformed into vector $\mathbf{u}$ in a different rectangular coordinate system as long as the rotation angles between the systems are known. It can be formalised as shown below:

$$\mathbf{u} = \mathbf{R} \cdot \mathbf{u}_0 \tag{6}$$

where $\mathbf{u}$ and $\mathbf{u}_0$ are the displacement vectors (components):

$$\mathbf{u} = \begin{bmatrix} U_1 \\ U_2 \\ U_3 \end{bmatrix}, \qquad \mathbf{u}_0 = \begin{bmatrix} U_x \\ U_y \\ U_z \end{bmatrix}.$$

Considering the properties of rotation matrix $\mathbf{R}$ (an orthogonal matrix with determinant 1), the inverse problem of (6) is:

$$\mathbf{u}_0 = \mathbf{R}^T \cdot \mathbf{u} \tag{7}$$

Considering the above, the displacement vectors can only be fully decomposed if three measurements in three linearly independent and non-coplanar directions are available.

In the case of a single satellite measurement (Fig. 2), the directional LOS displacement vector is known for point *P*. It is possible to compute the direction angles in the coordinate system with projections onto appropriate planes (*xy*, *xz*, *yz*) based on the coordinates of the satellite and the point on the ground.

A row of matrix **R** can be used to link the LOS vector to three vectors along the axes of the coordinate system.

When the displacement of point *P* is determined from two Sentinel-1 satellites on different orbits, two LOS vectors are obtained (Fig. 3).

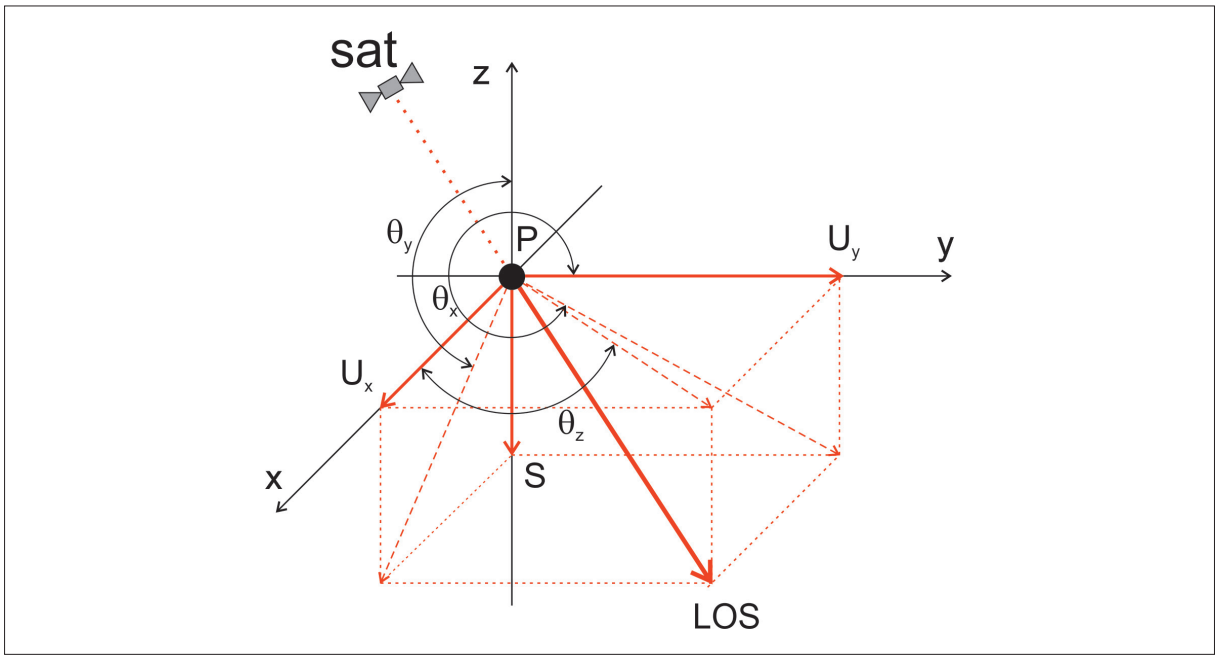

Fig. 2. *Direction angles of the LOS vector*

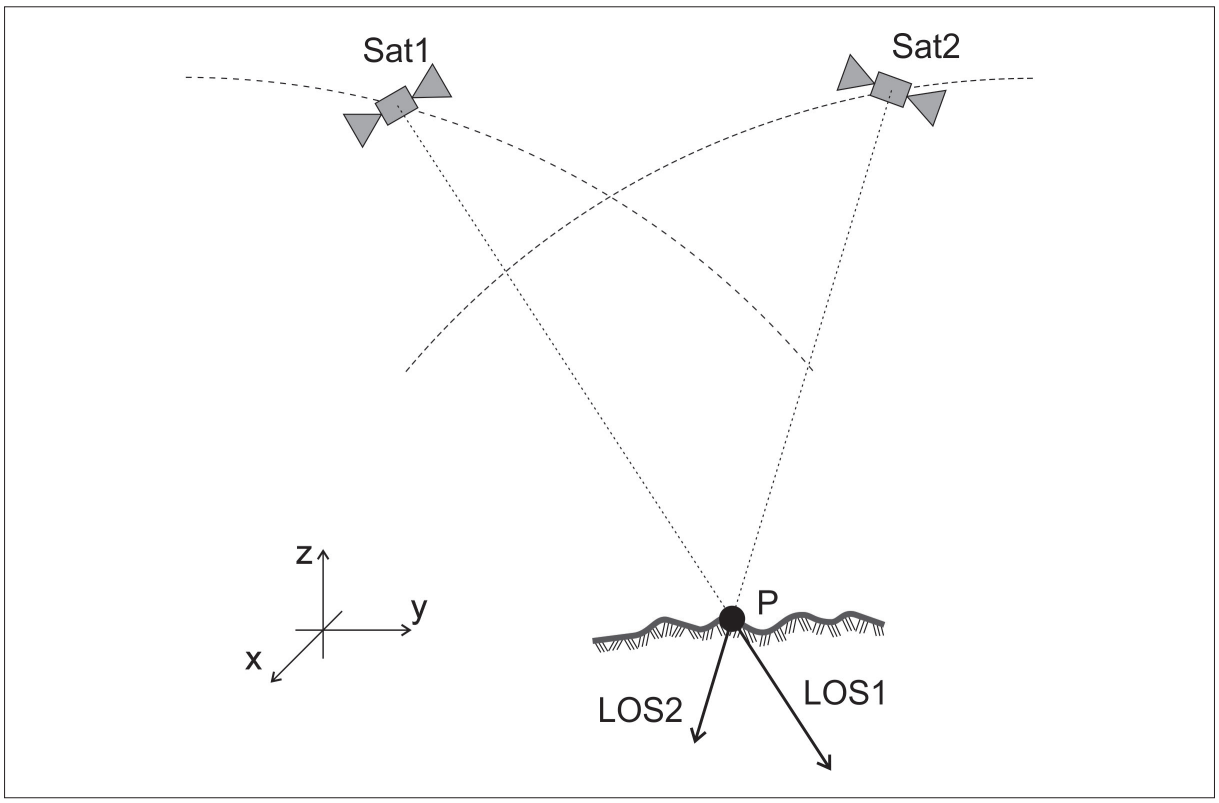

Fig. 3. *Displacement LOS vectors from two satellites*

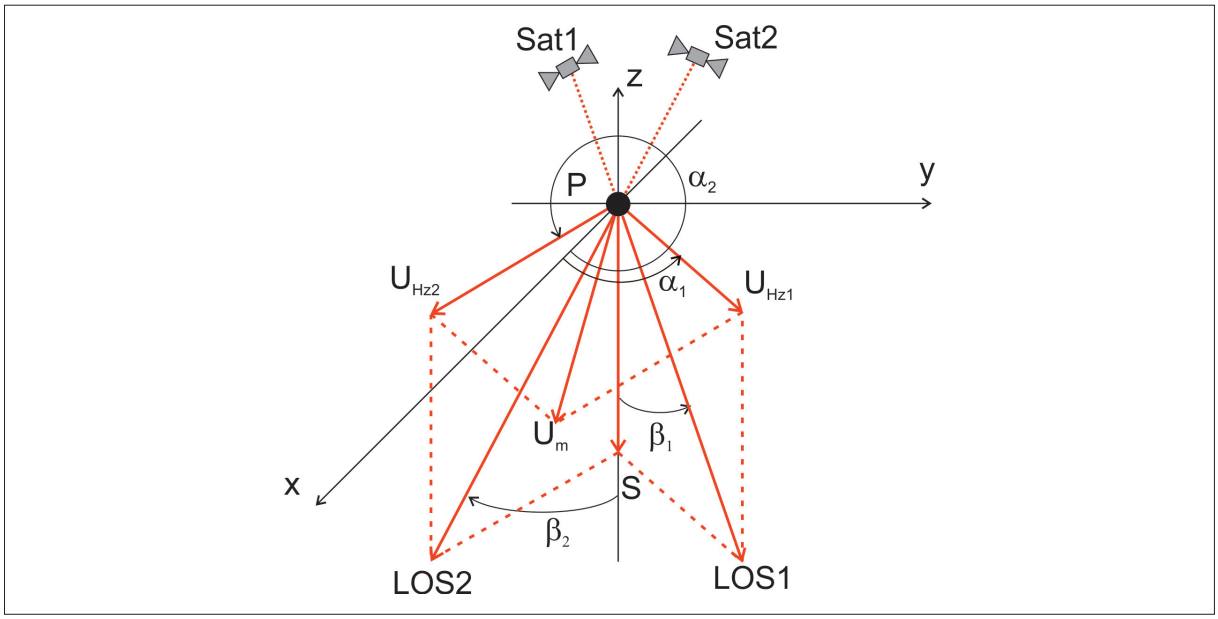

Fig. 4. *Decomposition of the LOS vector into two components*

It is impossible to fully decompose the two measured LOS vectors into their components in a three-dimensional rectangular coordinate system. They can only be decomposed into two components (Fig. 4): vertical S and horizontal U_m. Still, certain conditions apply. The calculations will be based on the third row of matrix **R** (5). New labels for the angles are introduced as shown in Figure 4:

- β is the angle on the vertical plane (on the z-axis and LOS vector) from the negative direction of the z-axis to the LOS vector measured counterclockwise (corresponding to the previous angle θ_y less 180 gon).
- α is the angle on the horizontal xy plane from the x-axis to the projection of the LOS vector on this plane measured counterclockwise.

Figures 2 and 4, the new labels, and rotation matrix **R** (the first row) yield the following system of equations:

$$\begin{cases} LOS_1 = -U_x \cdot \sin\beta_1 \cdot \cos\alpha_1 - U_y \cdot \sin\beta_1 \cdot \sin\alpha_1 + S \cdot \cos\beta_1 \\ LOS_2 = -U_x \cdot \sin\beta_2 \cdot \cos\alpha_2 - U_y \cdot \sin\beta_2 \cdot \sin\alpha_2 + S \cdot \cos\beta_2 \end{cases} \quad (8)$$

At this stage, two equations with three unknowns are present. When equations for the displacement vector on a plane are introduced, Equation (8) is transformed accordingly:

$$\begin{cases} LOS_1 = -U_{Hz1} \cdot \sin\beta_1 + S \cdot \cos\beta_1 \\ LOS_2 = -U_{Hz2} \cdot \sin\beta_2 + S \cdot \cos\beta_2 \end{cases} \quad (9)$$

Two vectors on the horizontal plane (U_{Hz1} and U_{Hz2}). The resultant vector can be determined as follows:

$$U_m = \sqrt{U_{Hz1}^2 + U_{Hz2}^2 + 2 \cdot U_{Hz1} \cdot U_{Hz2} \cdot \cos(\alpha_2 - \alpha_1)} \quad (10)$$

The number of unknowns can be reduced to two when the LOS vectors are perpendicular to each other or when their projections onto the horizontal plane have the same length. In the former case, the pair of vectors (LOS_1, LOS_2) can be transformed into the pair (U_m, S) using transformation matrices (1)–(3) or (5).

$$\mathbf{LOS}_1 \perp \mathbf{LOS}_2 \Rightarrow \begin{cases} LOS_1 = -U_m \cdot \sin\beta_1 + S \cdot \cos\beta_1 \\ LOS_2 = -U_m \cdot \sin\beta_2 + S \cdot \cos\beta_2 \end{cases} \quad (11)$$

The Equation (8) includes an assumption that the displacement in the x-direction is zero, considering the geometry of orbits in the Sentinel-1 system. It generates significant errors in locations where the reverse is true: the displacement along the x-axis is zero, and the displacement along the y-axis is substantial. Nevertheless, this assumption is universally employed.

The article contains a proposal of a possible solution for displacement fields induced by mining operations below.

GROUND DISPLACEMENT DUE TO MINING OPERATIONS

Over the last several decades, many methods and theories have been proposed for forecasting ground surface deformation from underground mining. These theories can be classified according to various criteria. One such classification can be summarised as (Chugh et al. 1989):

- empirical and semi-empirical methods (graphic, profiling functions, influence functions, zones);
- theoretical methods founded on continuum mechanics (elastic media, viscoelastic media, beam deflection);
- theories based on idealised models (stochastic model, diffusion model);
- numerical models (finite elements, boundary elements, discrete elements).

The most popular methods for forecasting displacement and deformation are the empirical and semi-empirical ones, particularly those based on influence functions. Therefore, a new assumption is introduced, stating that vertical displacement is determined using an influence function (Knothe 1953).

Consider a situation as shown in Figure 5. A mineral deposit on depth H has been extracted over area A. The mine void migrates towards the surface and emerges as an area of subsidence.

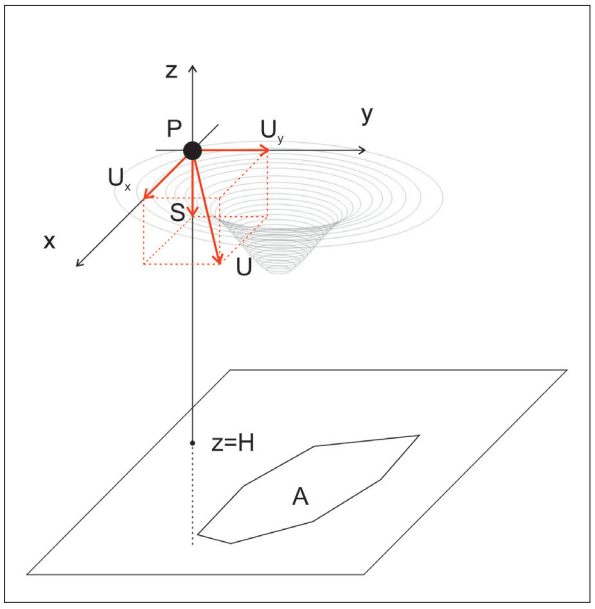

Fig. 5. *Subsidence from underground mining*

Points on the surface within the impact zone of the void are displaced and deformed. Figure 5 shows point P within the impact zone of the void. Using labels as per Figure 5, the vertical displacement S of this point can be described as:

$$S = S\iint_A f(x,y)\,dA_{\max} \tag{12}$$

where S_{max} is the maximum final subsidence [m], $f(x, y)$ is the influence function (theoretical function of influence infinitesimal elements of the excavation on subsidence), and A is the area of the extracted deposit.

In the initial period of interest in the adverse impact of mining, researchers focused solely on vertical displacement. Relationships to describe the horizontal movement of the ground were not sought until later. In general, there are three methods for describing a displacement field in the horizontal plane (Kwinta 2003):

1) a relationship Ψ between horizontal U and vertical displacement S, i.e.:

$$\Psi : S \to U,$$

2) a relationship Φ between horizontal displacement U and slopes of the subsidence trough profile T, i.e.:

$$\Phi : T \sim U,$$

3) independent determination of horizontal displacement, i.e.:

$$U := U(x,y).$$

Each group of the forecasting methods listed above offers interesting approaches. Methods in the second set are the most commonly employed, whereby horizontal displacement is described based on the profile slope of the subsidence trough. Avershin first made this observation. In fact, Avershin (1947) ascertained a relationship between horizontal deformations and curves as the following equation based on numerous measurements:

$$\frac{dU}{dx} - B\frac{d^2S}{dx^2} = 0 \tag{13}$$

where B is a coefficient of proportionality determined empirically.

The Equation (13) yields (integration) a commonly used relationship:

$$U_i = -B \cdot T_i \tag{14}$$

It means that horizontal displacement in any direction U_i is directly proportional to the slope of the subsidence trough profile T_i in that direction.

The value of the B coefficient has been widely investigated and discussed (for example, Hejmanowski & Kwinta 2009). The value is used in forecasting deformations, however, in the present study, Equation (14) is applied to calculate horizontal displacement in any direction α and the slope of the subsidence trough profile in that direction.

$$\begin{cases} T_\alpha = T_x \cdot \cos\alpha + T_y \cdot \sin\alpha \\ U_\alpha = U_x \cdot \cos\alpha + U_y \cdot \sin\alpha \end{cases} \tag{15}$$

i.e.:

$$\begin{cases} U_x = \dfrac{U_\alpha}{T_x \cdot \cos\alpha + T_y \cdot \sin\alpha} T_x \\ U_y = \dfrac{U_\alpha}{T_x \cdot \cos\alpha + T_y \cdot \sin\alpha} T_y \end{cases} \tag{16}$$

or as:

$$T_y \cdot U_x - T_x \cdot U_y = 0 \tag{17}$$

In this manner, an additional relationship between displacements in the horizontal plane can be introduced. Since the slope of the subsidence trough profile must first be calculated, the computation is performed using successive approximations. The procedure is outlined in the following section.

PROCEDURE OF VECTOR DECOMPOSITION

Based on the above theoretical solutions, the following procedure is proposed for decomposing LOS vectors in mining areas.

Two sets (tessellations) of LOS displacements from two different directions (e.g., two paths of Sentinel-1) are considered for an area affected by mining-induced deformation. The displacement is assumed to occur preferably across the entire subsidence trough. The coordinates of each point and the respective orientation angles relative to the coordinate system axes (the angle to the vertical axis and to the horizontal x-axis) are known for each LOS displacement.

In the initial step, approximate values of the displacement vector components U_{x0}, U_{y0}, $U_z = S$, are determined. According to Equation (8), the following applies:

$$\begin{cases} U_{x0} = \dfrac{\dfrac{LOS_1}{\cos\beta_1} - \dfrac{LOS_2}{\cos\beta_2}}{\mathrm{tg}\beta_2 \cdot \cos\alpha_2 - \mathrm{tg}\beta_1 \cdot \cos\alpha_1} \\ U_{y0} = 0 \\ S_0 = \dfrac{LOS_1 + U_{x0} \cdot \sin\beta_1 \cdot \cos\alpha_1}{2 \cdot \cos\beta_1} + \\ \quad + \dfrac{LOS_2 + U_{x0} \cdot \sin\beta_2 \cdot \cos\alpha_2}{2 \cdot \cos\beta_2} \end{cases} \tag{18}$$

The distribution of vertical displacements along the x and y axes of the coordinate system is subsequently integrated to determine the slope of the subsidence trough profile. When the displacement is regular and point density significant, the derivatives may be replaced with:

$$\begin{cases} T_x = \dfrac{\partial S_0}{\partial x} \approx \dfrac{\Delta S_0}{\Delta x} \\ T_y = \dfrac{\partial S_0}{\partial y} \approx \dfrac{\Delta S_0}{\Delta y} \end{cases} \tag{19}$$

Subsequently, Equations (8) and (17) are used to construct a system represented in the form of a matrix equation:

$$\begin{bmatrix} LOS_1 \\ LOS_2 \\ 0 \end{bmatrix} = \begin{bmatrix} -\sin\beta_1 \cdot \cos\alpha_1 & -\sin\beta_1 \cdot \sin\alpha_1 & \cos\beta_1 \\ -\sin\beta_2 \cdot \cos\alpha_2 & -\sin\beta_2 \cdot \sin\alpha_2 & \cos\beta_2 \\ T_y & -T_x & 0 \end{bmatrix} \cdot \begin{bmatrix} U_x \\ U_y \\ S \end{bmatrix} \tag{20}$$

Equation (20) can be solved with matrix calculus, but in some cases, the matrix is ill-definite (very small elements).

The problem can also be approached differently. Based on displacement and slope along the x-axis of the coordinate system and using Equation (14), the mean value of the proportionality coefficient between horizontal displacement and subsidence trough profile slope is determined:

$$B_m = \frac{1}{n} \sum_{i=1}^{n} \frac{-U_{x0}}{T_x} \tag{21}$$

Then, the mean value is used to calculate the components of the displacement vectors:

$$\begin{cases} U_x = -B_m \cdot T_x \\ U_y = -B_m \cdot T_y \\ S = \dfrac{LOS_1 + \left(U_y \cdot \sin\alpha_1 + U_x \cdot \cos\alpha_1\right) \cdot \sin\beta_1}{2 \cdot \cos\beta_1} + \\ \quad + \dfrac{LOS_2 + \left(U_y \cdot \sin\alpha_2 + U_x \cdot \cos\alpha_2\right) \cdot \sin\beta_2}{2 \cdot \cos\beta_2} \end{cases} \quad (22)$$

Considering that the calculations start with the determining approximate values of the displacement vectors, the iterative method is preferable for obtaining their final values.

Consequently, a convergence metric must be defined to terminate the iteration process. For the purposes of this article, the following metric is assumed as the metric of changes in displacement from the iteration process:

$$\Delta = \sqrt{\left(U_x - U_{x0}\right)^2 + \left(U_y - U_{y0}\right)^2 + \left(S - S_0\right)^2} \quad (23)$$

The metric (23) can be considered the stopping criterion for the iteration process. The iteration process is repeated with the displacement component values calculated in the previous step used as approximate values of the components. The computation cycle (19) through (23) is then repeated until the limit value of the Δ metric is achieved.

The method yields three components of displacement vectors for ground surface affected by mining operations. The proposed solution is verified with a few cases below.

CASE SCENARIOS

The soundness of the solution to the problem posed above is tested with calculations for a few cases:

1) a theoretical (blind) case based on generated theoretical (model) displacement values;
2) cases of continuous short-term tremor-induced displacements over a room-and-pillar copper ore mine.

Theoretical case scenario

The best verification method for computation algorithms is a blind case. A hypothetical mining area of defined dimensions is modelled, generating the maximum possible vertical displacement over its centre. The assumed extraction method is longwall mining with caving. There is a 2,000 m × 2,000 m point grid over the mining zone. The mesh size is 20 m × 20 m. The deformation is determined for 10,201 points. An overview of the mining area and the points is shown in Figure 6.

The outline of the mining zone is marked in red in Figure 6, and grid points are in black. Deformation coefficients were calculated according to the Knothe–Budryk theory in the Modez 4 deformation modelling software (Hejmanowski & Kwinta 2010). The theoretical values of displacement vectors were determined based on the specified data and parameters (Fig. 6). The mining field was configured so that the maximum displacement was over its centre and the displacements cancelled each other on the edges of the grid. The theoretical values of displacements along the *x*-axis reach the maximum, while displacements along the *y*-axis reach zero on the midpoint of the vertical edge of the mining field. Conversely, displacements in the *x*-direction are zero and horizontal displacements along the *y*-axis reach maximum values on the horizontal edge. The generated displacements are shown in Figure 7. Next, two hypothetical locations of satellites and imaging parameters (horizontal and vertical angles) were assumed, and displacements of LOS_1 and LOS_2 were determined according to Equation (8). The displacements are represented in Figure 7.

As per the procedure in section "Procedure of vector decomposition", vectors LOS_1 and LOS_2 LOS_1 were employed to compute displacement field vectors iteratively. Table 1 shows the values of the distance parameter Δ (23) for consecutive iterations from the table. It also contains the maximum divergence between the approximate and computed displacement vectors for each coordinate system axis and for entire vectors.

Table 1
Results of consecutive calculations of the displacement vector variability measure for the theoretical case scenario

Calculation	Δ*S* [mm]	ΔU_x [mm]	Δ*Uy* [mm]	Δ$_{max}$ [mm]
Classical	116.5	47.8	971.6	978.5
Iteration 1	9.7	54.4	80.2	80.8
Iteration 2	3.3	15.0	27.4	27.6
Iteration 3	0.4	1.5	3.4	3.4

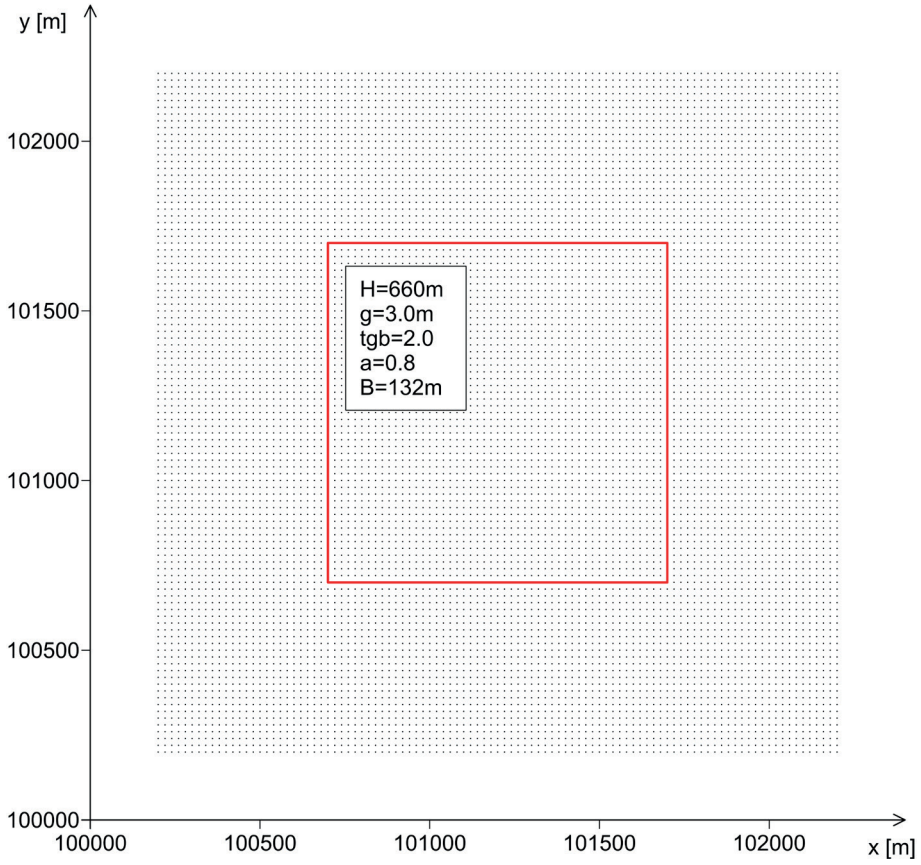

Fig. 6. *Graphical summary of data for the theoretical example*

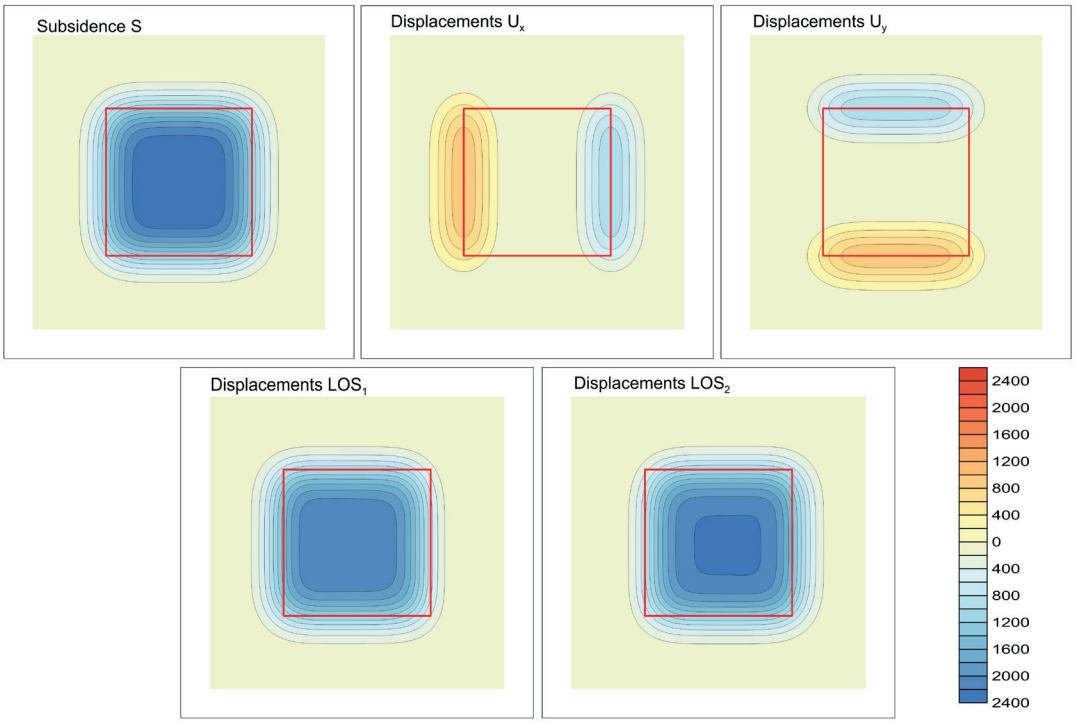

Fig. 7. *Theoretical displacement vectors*

The results in Table 1 demonstrate that the most significant changes in displacement vectors occur for horizontal displacements in the *y*-direction of the coordinate system. The values are large for the classical calculation, which is only to be expected considering the assumption of no displacement in that direction. Still, this assumption also generates errors for the remaining components of the displacement field. In this case, the other displacement differences are also significant, which shows that the assumption of no displacement along the *y*-axis is wrong. The differences decline with each consecutive iteration. The iteration process is terminated when the result is satisfactory. Figure 8 shows distributions of differences between the calculated vectors for classical and iterative calculations and the theoretical (input) values of displacement.

The results shown in Table 1 and Figure 8 unambiguously confirm that the proposed algorithm is correct. The algorithm is now verified against real-life cases, based on DInSAR measurements.

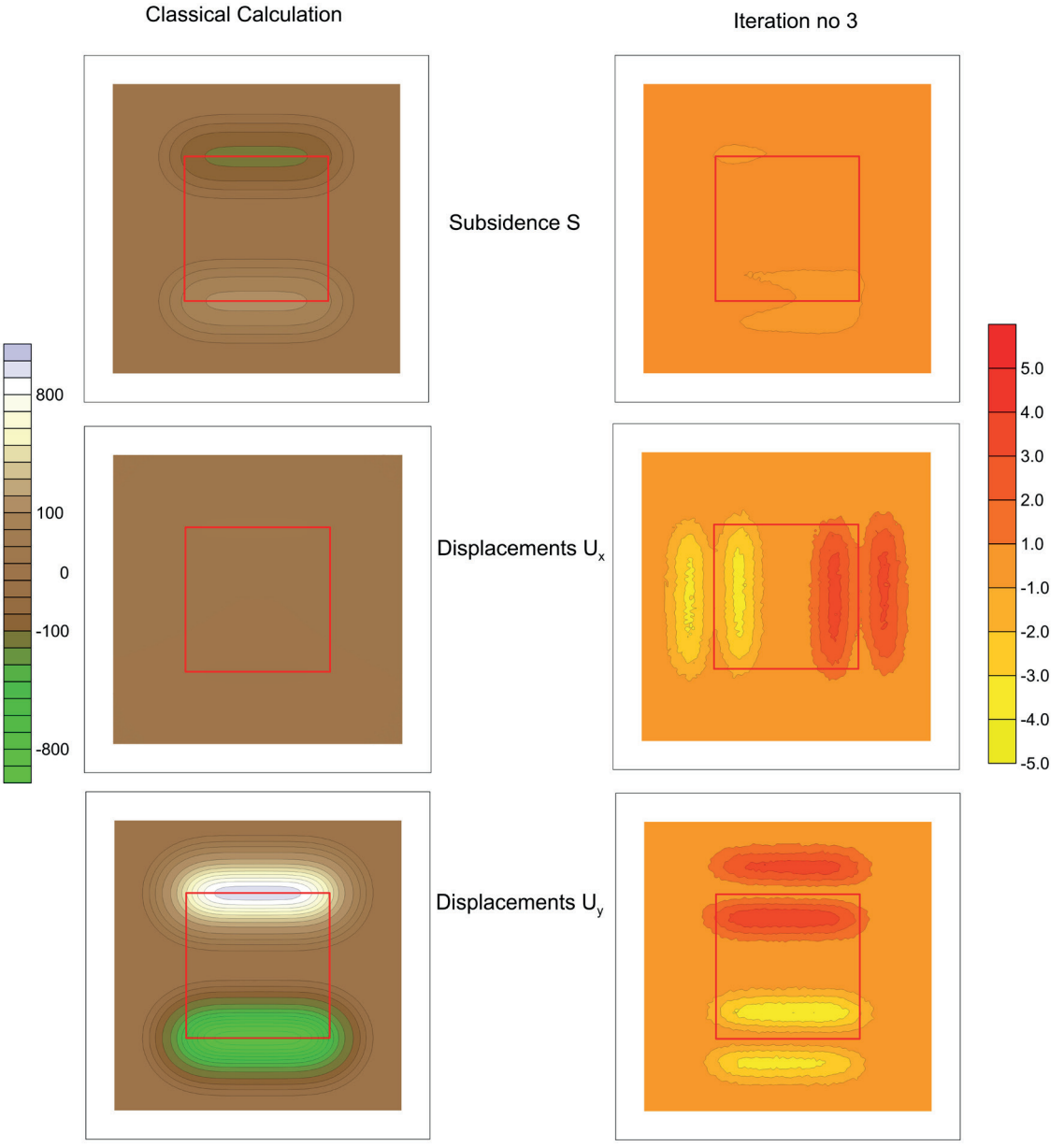

Fig. 8. *Divergences between theoretical and calculated values of displacement vectors*

REAL-LIFE CASE SCENARIOS

It was demonstrated above that the algorithm works with a theoretical case scenario. Now, the algorithm was tested using real-life data. As previously mentioned, three real-life cases of copper ore mining subsidence were selected. All of the cases were dynamic events (mining-induced tremors) from 2016 to 2017 in the area of the LGCD. SAR images from Sentinel-1A/B platforms, from two orbits (ascending and descending) were available for the area at that time so that LOS vectors could be decomposed, and the impact of the tremors on ground surface displacement determined (Malinowska et al. 2018, Owczarz & Blachowski 2020, Milczarek et al. 2021). We selected SAR images with the shortest time interval for each event. Details of the SAR data used for determining LOS vectors for each case are shown in Table 2.

DInSAR LOS displacements were determined in GMTSAR software (Sandwell et al. 2011), phase unwrapping was carried out using the SNAPHU algorithm (Chen & Zebker 2002). GACOS atmospheric correction was also applied (Yu et al. 2018).

Figures 9–11 present (top-down):

- spatial distributions of the LOS vectors;
- the position of the tremor against the outline of the mining area and distribution of vertical displacement as determined here;
- subsidence trough profile slopes towards the axes of the coordinate system;
- determined horizontal displacements along the axes of the coordinate system.

All the distribution diagrams in Figures 9–11 were made in SURFER following appropriate interpolation methods in grids. The subsidence trough profile slopes were also computed with a dedicated function in SURFER.

Data in Figure 9 demonstrate that the subsidence trough is well developed around the epicentre of the induced tremor (the red star). The displacement image is rather regular as both LOS vectors have similar values and shapes.

Concerning the second case shown in Figure 10, there were some analytical challenges. The first issue was that two tremors occurred on the same day, not far from each other. Therefore, the bottom of the subsidence trough is not over the epicentres, but rather shifted towards the mine void. The distribution of the LOS vectors shows significant disproportions of deformations. The maximums for the LOS_2 vector are over twice the values of the maximums of the LOS_1 vector and this is detrimental to the shape of the subsidence trough. Therefore, the subsidence trough profile slopes are irregular, resulting in an irregular distribution of horizontal displacements.

Table 2
The data concerning SAR images and tremors dates and times

Case	Dates and times of tremors [dd-mm-yyyy, hh:mm:ss (UTC)]	Image	SAR images acquisition dates and times [dd-mm-yyyy, hh:mm:ss (UTC)]	
			ascending path	descending path
1	17-10-2016 23:50:32	reference	11-10-2016 16:43:32	08-10-2016 05:08:48
		secondary	23-10-2016 16:43:32	20-10-2016 05:08:48
2	16-12-2016 06:46:51	reference	10-12-2016 16:43:31	13-12-2016 05:08:02
		secondary	16-12-2016 16:43:31	19-12-2016 05:08:47
3	07-12-2017 17:42:50	reference	05-12-2017 16:43:341	02-12-2017 05:08:59
		secondary	17-12-2017 16:43:33	14-12-2017 05:08:68

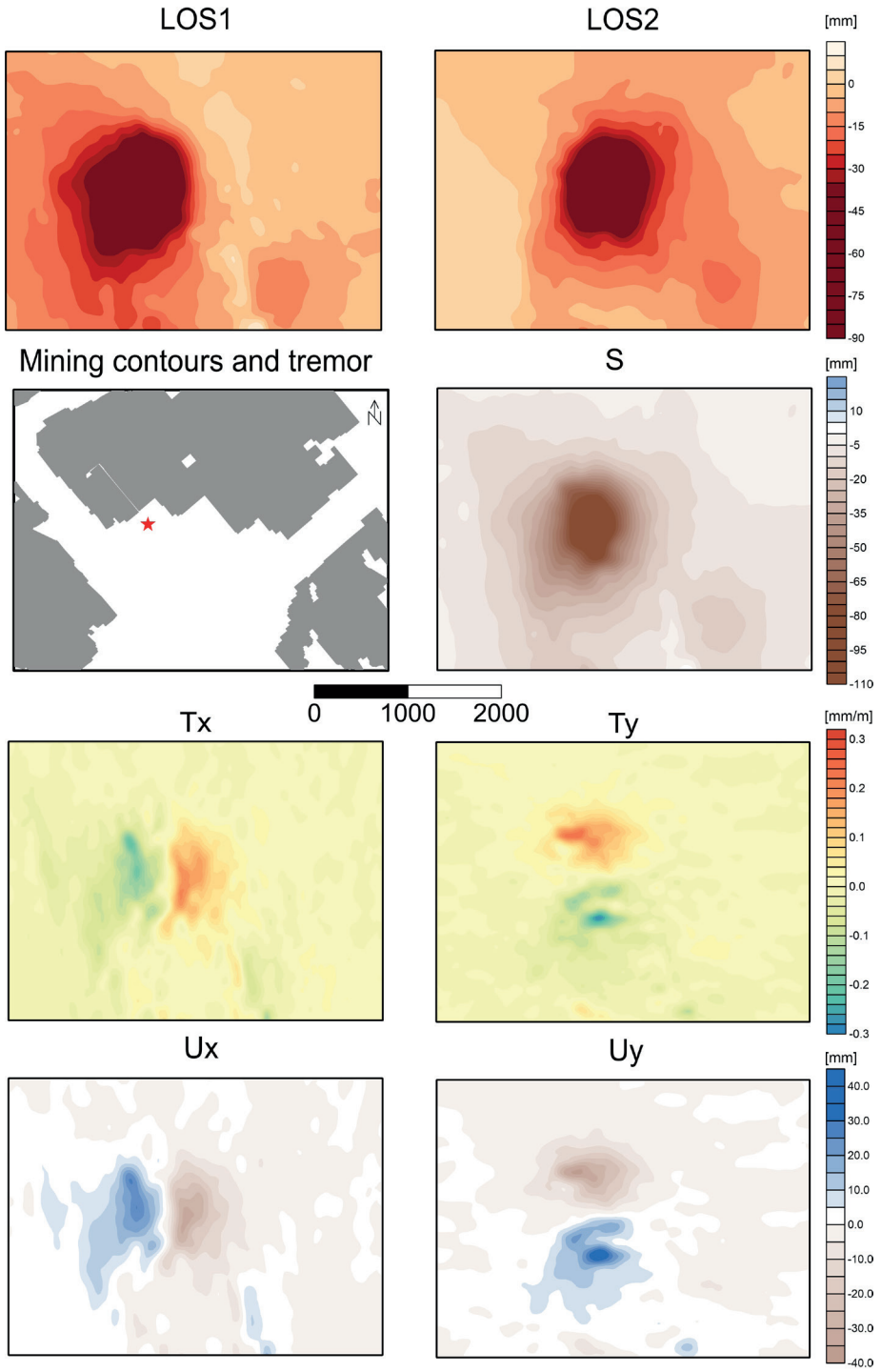

Fig. 9. *Results of LOS vectors decomposition – case 1*

The third case in Figure 11 is also far from 'perfect'. The LOS vectors only reach the maximum values near the lower edge of the image. Here, the LOS vectors are also disproportionate. The bottom of the subsidence trough is located near the epicentre, but regrettably, only the bottom and the northern part of the trough had been recorded. That is why the image of slopes and horizontal displacements is incomplete in this case. The small subsidence trough in the top right corner of the image is interesting.

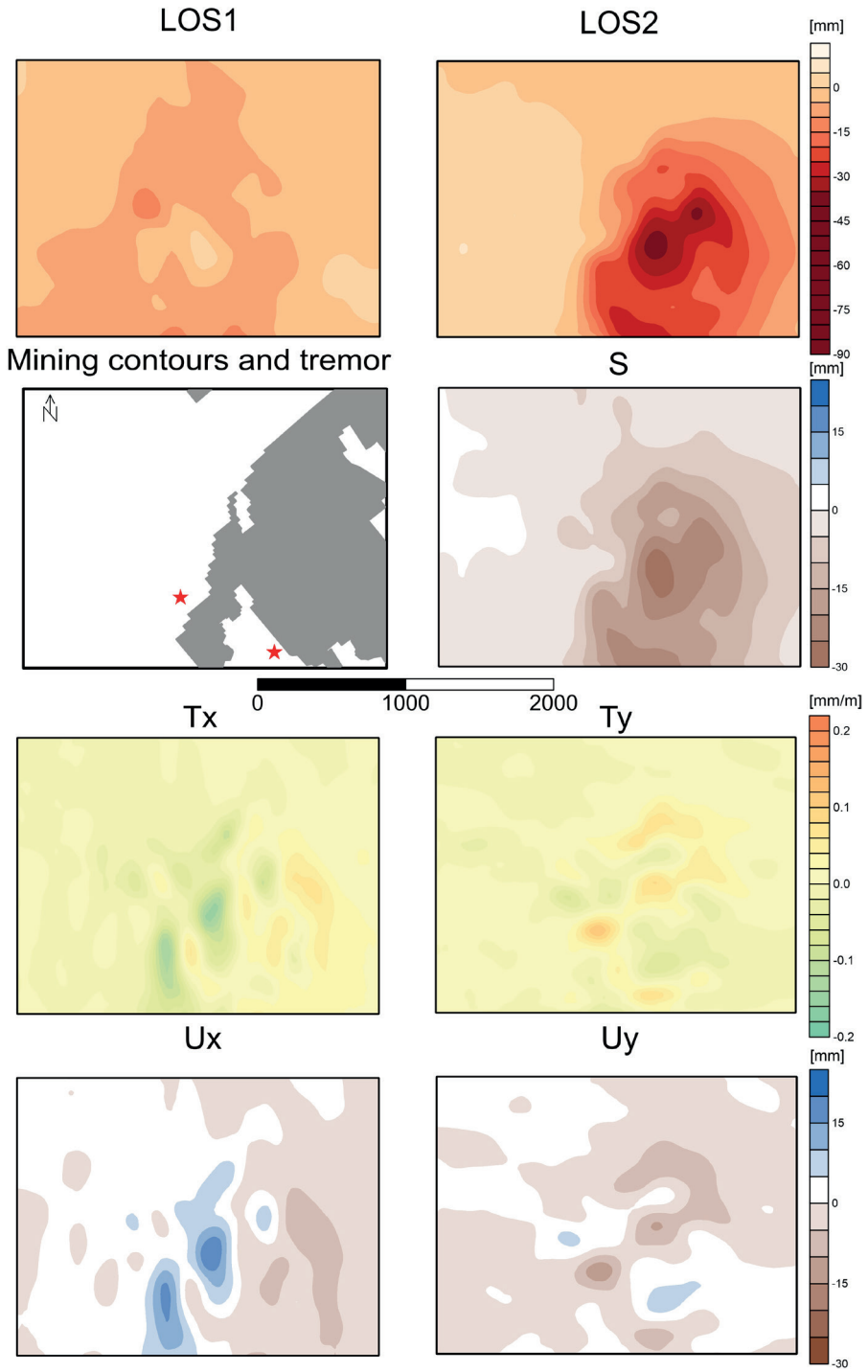

Fig. 10. *Results of LOS vectors decomposition – case 2*

The maximum displacement on the bottom of that trough is about 18 mm, but it is regular and can be found in both LOS images. Its slopes are regular, leading to relatively regular horizontal displacements of about 12 mm for the *x*-axis and 14 mm for the *y*-axis. It supports the notion that 'good' LOS imaging allows the researcher to identify regular troughs and determine the 'smooth' distributions of horizontal displacements.

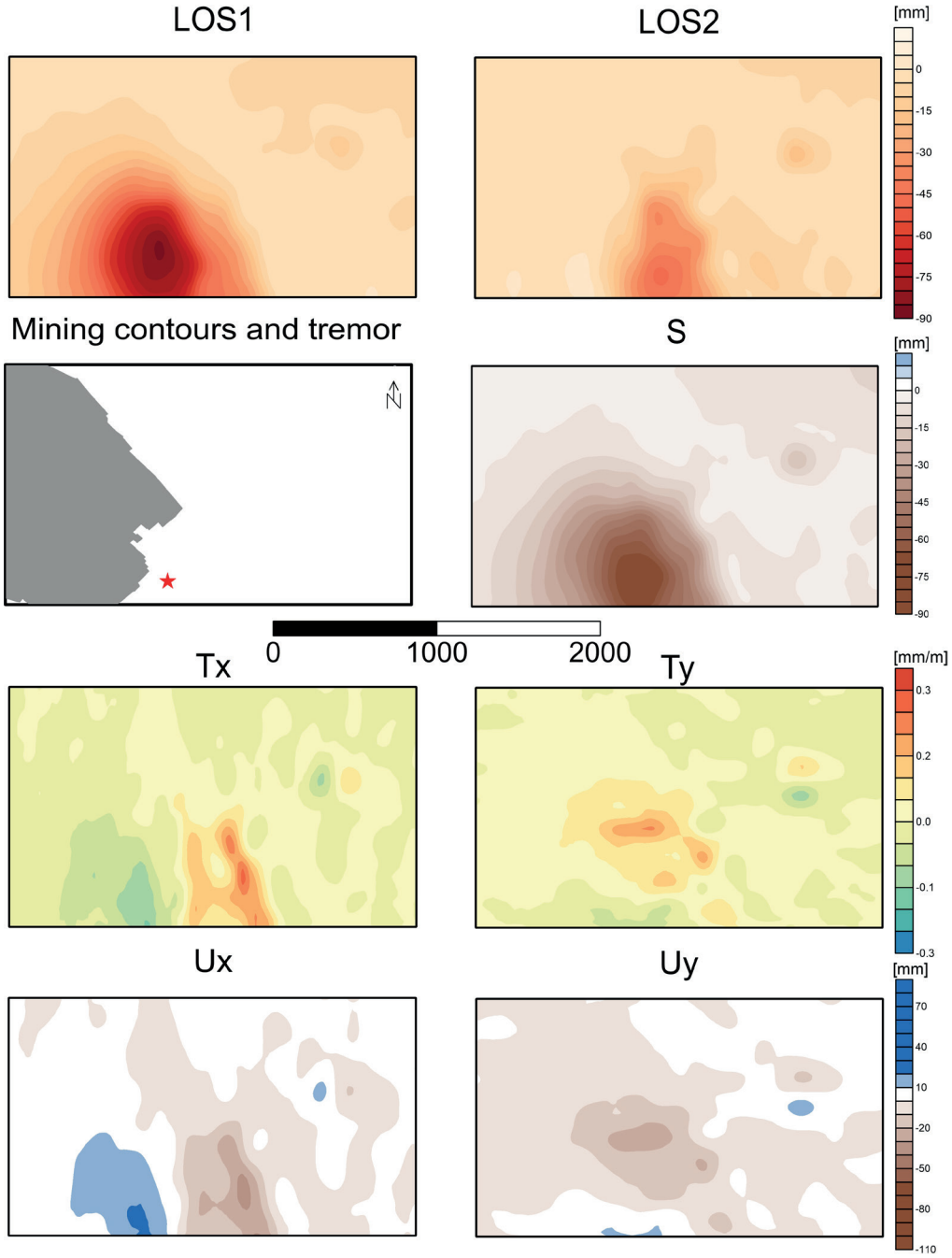

Fig. 11. *Results of LOS vectors decomposition – case 3*

ANALYSIS AND DISCUSSION OF THE RESULTS

As demonstrated in the theoretical part, redundant observations are required to accurately represent a displacement field, similarly to classical survey methods. Three non-collinear observations are the minimum number of observations necessary to determine a spatial displacement vector. A system of three independent measurements can determine three displacement vector components. Still, when measurements contain errors (all measurements do), the end result may be incorrect. Every redundant measurement improves

the accuracy of the calculated displacement values. The matter is even worse when the number of observations is lower than the number of displacements to be calculated. When only a single DInSAR LOS vector is available, only the slant vectors can be analysed, and no inference regarding the components of the displacement field can be made. In the case of two slant LOS vectors, additional information about displacement values is available; however, the third observation remains unavailable. If the deformation occurs only in two dimensions and the LOS vectors are coplanar, the components of a two-dimensional displacement field can be computed. Deformations in mining areas, whether direct, indirect, or secondary, are spatial displacements described with three components. Hence, when two images are available, the system is underdetermined. Decomposing two LOS vectors into two components and assuming a zero value of the third component may be a grave mistake. This conundrum can be resolved (at least for mining areas) with the observation that horizontal displacements are proportionate to the slopes of the subsidence trough profile (the Avershin observation). The observation offers an additional equation, but slopes can only be calculated if vertical displacement is known, hence the need for an iterative algorithm.

The algorithm proposed in section "Procedure of vector decomposition" was tested on a theoretical case and three practical cases. The theoretical (blind) case made it possible to verify whether the algorithm was correctly constructed and produces accurate results. The results are indeed consistent with the input data. Therefore, the algorithm works.

The next step was to test the solution in real-life cases. Small and dynamic subsidence troughs caused by induced tremors near underground mining sites were selected for analysis. In this case, the void in the rock mass reaches the surface faster due to vibrations than in the case of direct deformation processes. Figures 12–14 show isolines of the differences between the classical displacement computation method (in two directions) and the displacements computed using the algorithm.

The graphs include contours of the mine operation areas and epicentres of the tremors that shaped the subsidence troughs. Each case demonstrates significant differences in terms of values and ranges. Table 3 summarises the depth of the tremor H, the calculated mean proportionality coefficient B_m, and the maximum difference between vectors calculated with the two methods for each case.

Table 3
Summary of results of calculations for each real-life case scenario investigated

Case	H [m]	B_m [m]	Δ [mm]
1	984	173.97	45.6
2	954	167.67	40.5
3	935	172.28	53.8

Our results confirm that the classical method for decomposing LOS vectors generates significant axis value errors (in the directions of axes of the coordinate system) for displacement vectors. When the iterative algorithm and additional equation are employed, the displacement representation is more consistent with actual values than for classical computations. Data in Table 3 offer one more interesting insight. Values of the proportionality coefficient are similar in each case. The tremor epicentres were also at similar depths. Standardisation of the proportionality coefficient B_m in relation to H yields a value of approx. $0.18H$, which is consistent with the value proposed by Avershin (1947) and coefficient values calculated for classical surveying methods and analyses on survey lines (Hejmanowski & Kwinta 2009).

Underground mining operations cause voids that migrate upwards and create subsidence troughs. Describing the geometry of subsidence troughs is challenging because of the limited number of observations and the complex origin of the troughs driven by many mining and geological factors. Analyses are hampered by the fact the various influences overlap, disturbing the course, time, and shaping of subsidence troughs in space. Classical surveying methods offer very limited capabilities for measuring trough geometry because of their temporal and spatial discreteness, as indicated also by other research teams in their publications, e.g. Yang et al. (2020) and Przyłucka et al. (2024).

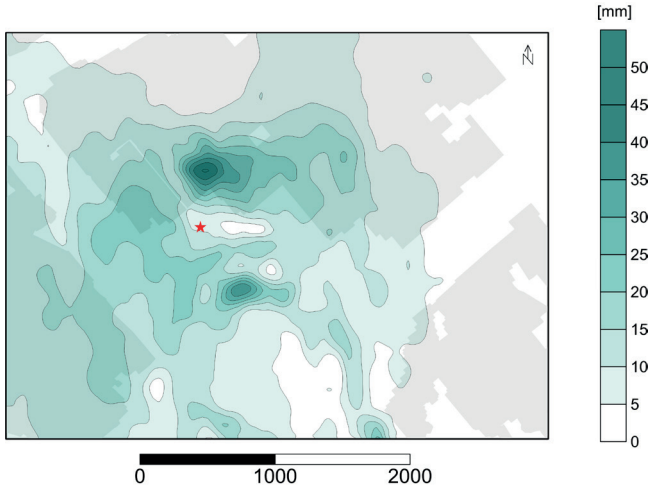

Fig. 12. *Distribution of differences Δ (23) between displacement vectors for case 1*

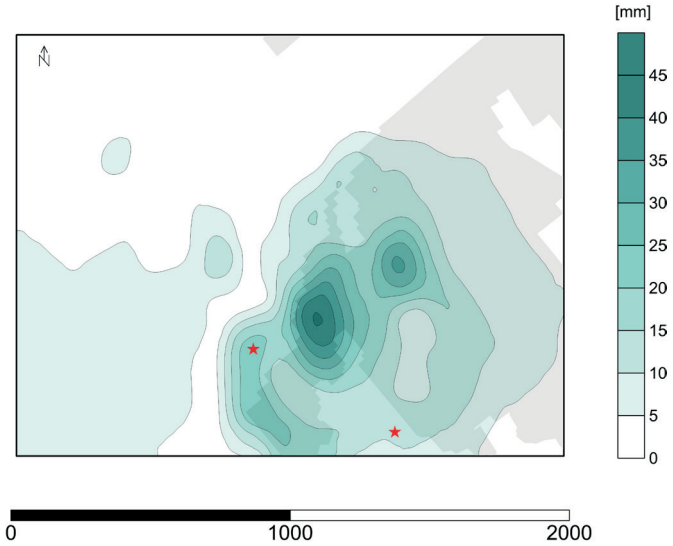

Fig. 13. *Distribution of differences Δ (23) between displacement vectors for case 2*

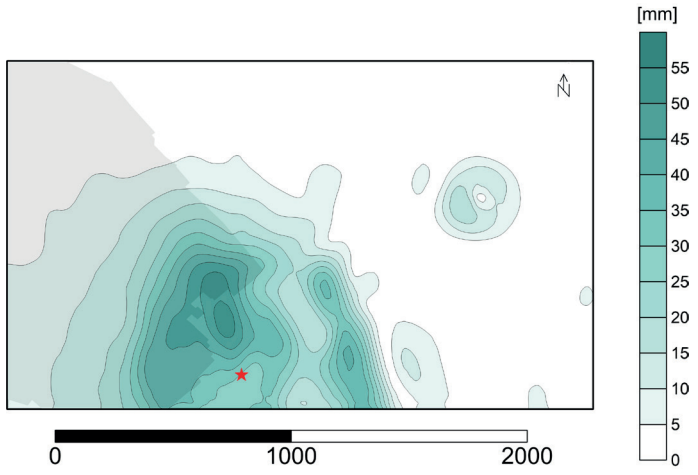

Fig. 14. *Distribution of differences Δ (23) between displacement vectors for case 3*

Interferometric synthetic aperture radar techniques revolutionised the computation of displacement vectors. They can provide data on ground surface point displacement for large areas affected by mining in a relatively short time.

Regrettably, classical methods for decomposing LOS (two LOS vectors into three vectors along of the coordinate system) vectors generate displacement errors along axes of the coordinate system. If the number of measured vectors is insufficient relative to the number of vectors being calculated, a significant problem arises. It can be helped by using an observation of the proportionality of displacements in the vertical and horizontal planes. The present article proposes an iterative algorithm for solving the problem. Our analyses of theoretical and real-life case scenarios demonstrate the substantial computational capabilities of the algorithm. Differences between classically and iteratively computed displacement vectors are important for correctly describing the deformation process. This is a solution that can be classified as a combined method, integrating geometric and physical approaches (Brouwer & Hanssen 2024). Unlike other proposed methods, such as pixel offset (Chen et al. 2018) or inversion-based (Tang et al. 2019, Brouwer & Hanssen 2024), the proposed solution is characterized by simplicity, due to the small number of parameters. It makes the solution easy to implement in practice and systematic errors are reduced. The proposed method, due to the possibility of adjusting the parameters to different types of mining operations, can be used for the decomposition of the LOS vector in various areas affected by mining activities.

New satellite technologies are promising and it seems merely a matter of time before an observed area can be assigned to a network of a dozen or so SAR sensors that will represent changes in a spatial displacement field induced by mining operations in real time. Several satellites will help compute displacement and analyse the accuracy of end results. Until then, it seems reasonable to employ the iterative algorithm proposed in this study. It should be noted that the presented method has limitations resulting from, among others: accuracy limitations of SAR images, deformation process disturbances, overlap of several causes. The algorithm can also be used to determine the coefficient of proportionality between horizontal displacement and subsidence trough profile slopes for an area of mining operations, which is relevant to ground surface deformation forecasting.

CONCLUSIONS

In summary, this work introduces a novel approach for resolving underdetermined decomposition problems in SAR-based displacement monitoring. By leveraging domain-specific knowledge of mining-induced ground behaviour, the method bridges classical theory with the modern InSAR technique. It represents a meaningful contribution to the field of ground surface deformation monitoring and has promising applicability in various mining areas.

Based on the research and analyses conducted in this work, the following conclusions can be drawn:

- Determining 3D displacements based on two LOS measurements without additional constraints leads to significant directional errors in displacement estimation especially in north – south direction.
- In mining areas where deformations follow known empirical behaviour, it is possible to incorporate an additional equation to close the equation and achieve more accurate decomposition.
- The proposed iterative method successfully integrates the Avershin relation into InSAR analysis and provides a computationally effective tool for estimating spatial displacements.
- For the LGCD area, the proportionality assumption holds and improves results; in the case of tremor-induced deformations, the algorithm demonstrates particularly high reliability.
- The method also enables the estimation of parameters relevant to generalized Knothe models – B_m, which are valuable for forecasting surface deformation.

Work on this issue is ongoing.

REFERENCES

Avershin S.G., 1947. *Sdvizheniye gornykh porod pri podzemnykh razrabotkakh* [Displacement of rock masses during underground mining]. Ugletekhizdat, Moskva.

Blachowski J., Milczarek W. & Stefaniak P., 2014. Deformation information system for facilitating studies of mining ground deformations – development and applications. *Natural Hazards and Earth System Sciences*, 14(7), 1677–1689. https://doi.org/10.5194/nhess-14-1677-2014.

Blachowski J., Jiránková E., Lazecký M., Kadlečík P. & Milczarek W., 2018. Application of satellite radar interferometry (PSInSAR) in analysis of secondary surface deformations in mining areas: Case studies from Czech Republic and Poland. *Acta Geodynamica et Geomaterialia*, 15(2), 173–185. https://doi.org/10.13168/AGG.2018.0013.

Brouwer W.S. & Hanssen R.F., 2024. Estimating three-dimensional displacements with InSAR: The strapdown approach. *Journal of Geodesy*, 98(12), 110. https://doi.org/10.1007/s00190-024-01918-2.

Camós C. & Molins C., 2015. 3D analytical prediction of building damage due to ground subsidence produced by tunneling. *Tunnelling and Underground Space Technology*, 50, 424–437. https://doi.org/10.1016/j.tust.2015.08.012.

Castellazzi P., Arroyo-Domínguez N., Martel R., Calderhead A.I., Normand J.C., Gárfias J. & Rivera A., 2016. Land subsidence in major cities of Central Mexico: Interpreting InSAR-derived land subsidence mapping with hydrogeological data. *International Journal of Applied Earth Observation and Geoinformation*, 47, 102–111. https://doi.org/10.1016/j.jag.2015.12.002.

Chang Z., Yu W., Wang W., Zhang J., Liu X. & Zhu J. 2017. An approach for accurately retrieving the vertical deformation component from two-track InSAR measurements. *International Journal of Remote Sensing*, 38(6), 1702–1719. https://doi.org/10.1080/01431161.2017.1285448.

Chen B.Q., Jiang D., Zhang J., Gao J. & Fan X.T., 2018. Monitoring of 3D large surface deformation in coal mines through the integration of synthetic aperture radar pixel offset tracking and probability integration function model. *Instrumentation, Mesure, Métrologie*, 17(3), 507–519. https://doi.org/10.3166/I2M.17.507-519.

Chen C.W. & Zebker H.A., 2002. Phase unwrapping for large SAR interferograms: Statistical segmentation and generalized network models. *IEEE Transactions on Geoscience and Remote Sensing*, 40(8), 1709–1719. https://doi.org/10.1109/TGRS.2002.802453.

Chugh Y.P., Hao Q.-W. & Zhu F.-S., 1991. State-of-the-art in mine subsidence prediction. [in:] Singh B. & Saxena N.C. (eds.), *Land Subsidence: Proceedings of the International Symposium, Dhanbad, India, 11–15 December 1989*, A.A. Balkema, Rotterdam, 51–66.

Cigna F. & Tapete D., 2022. Urban growth and land subsidence: Multi-decadal investigation using human settlement data and satellite InSAR in Morelia, Mexico. *Science of the Total Environment*, 811, 152211. https://doi.org/10.1016/j.scitotenv.2021.152211.

Dittrich J., Hölbling D., Tiede D. & Sæmundsson Þ., 2022. Inferring 2D local surface-deformation velocities based on PSI analysis of Sentinel-1 data: A case study of Öræfajökull, Iceland. *Remote Sensing*, 14(13), 3166. https://doi.org/10.3390/rs14133166.

Dong L., Wang C., Tang Y., Tang F., Zhang H., Wang J. & Duan W., 2021. Time series InSAR three-dimensional displacement inversion model of coal mining areas based on symmetrical features of mining subsidence. *Remote Sensing*, 13(11), 2143. https://doi.org/10.3390/rs13112143.

Galloway D. & Burbey T., 2011. Review: regional land subsidence accompanying groundwater extraction. *Hydrogeology Journal*, 19(8), 1459–1486. https://doi.org/10.1007/s10040-011-0775-5.

Ge L., Chang H.-C. & Rizos C., 2007. Mine subsidence monitoring using multi-source satellite SAR images. *Photogrammetric Engineering & Remote Sensing*, 73(3), 259–266. https://doi.org/10.14358/PERS.73.3.259.

Hejmanowski R. & Kwinta A., 1997. Implementation of GPS satelitary technique for monitoring of point displacements on mining areas. [in:] *Second World Mining Environment Congress WOMEC '97: 13–16 May 1997, Katowice, Poland: Proceedings. Vol. 1*, CMI, Katowice, 351–369.

Hejmanowski R. & Kwinta A., 2001. Measurement of horizontal displacements in European coalfields. [in:] *10th International Symposium on Deformation Measurements: Orange, California, USA 19–22 March 2001: [abstracts]*, 31–39.

Hejmanowski R. & Kwinta A., 2009. Determining the coefficient of horizontal displacements with the use of orthogonal polynomials. *Archives of Mining Sciences*, 54(3), 441–454.

Hejmanowski R. & Kwinta A., 2010. Modelowanie deformacji ciągłych powierzchni terenu w warunkach zmiennego zalegania złoża. *Gospodarka Surowcami Mineralnymi = Mineral Resources Management*, 26(3), 143–153.

Karimzadeh S., Ghasemi M., Matsuoka M., Yagi K. & Zulfikar A.C., 2022. A deep learning model for road damage detection after an earthquake based on synthetic aperture radar (SAR) and field datasets. *IEEE Journal of Selected Topics in Applied Earth Observations and Remote Sensing*, 15, 5753–5765. https://doi.org/10.1109/JSTARS.2022.3189875.

Knothe S., 1953. Równanie profilu ostatecznie wykształconej niecki osiadania. *Archiwum Górnictwa i Hutnictwa*, 1(1), 22–38.

Kopeć A., 2021. *Metodyka przetwarzania danych interferometrycznych w aspekcie oddziaływania podziemnej eksploatacji górniczej na powierzchnię terenu*. Politechnika Wrocławska. Wrocław [PhD thesis].

Kratzsch H., 1983. *Mining Subsidence Engineering*. Springer, Berlin, Heidelberg, New York.

Kwinta A., 2003. *Weryfikacja modeli niestacjonarnego pola poziomych przemieszczeń górniczych*. Akademia Górniczo-Hutnicza, Kraków [PhD thesis].

Litwiniszyn J., 1974. A remark concerning the so called "point of the attraction centre" and its connection with the formation of the subsidence trough. *Archiwum Górnictwa*, 19(3), 231–236.

Loupasakis C., Angelitsa V., Rozos D. & Spanou N., 2014. Mining geohazards – Land subsidence caused by the dewatering of opencast coal mines: The case study of the Amyntaio coal mine, Florina, Greece. *Natural Hazards*, 70(1), 675–691. https://doi.org/10.1007/s11069-013-0837-1.

Malinowska A., Witkowski W., Guzy A. & Hejmanowski R., 2018. Mapping ground movements caused by mining-induced earthquakes applying satellite radar interferometry. *Engineering Geology*, 246, 402–411. https://doi.org/10.1016/j.enggeo.2018.10.013.

Milczarek W., Kopeć A., Głabicki D. & Bugajska N., 2021. Induced seismic events – distribution of ground surface displacements based on InSAR methods and Mogi and Yang models. *Remote Sensing*, 13(8), 1451. https://doi.org/10.3390/rs13081451.

Niemczyk O., 1935. Zur Frage des Grenz- und Bruchwinkels bei Bodensenkungen. *Mitteilungen aus dem Markscheidewesen*, 46, 37–48.

Owczarz K. & Blachowski J., 2020. Application of DInSAR and spatial statistics methods in analysis of surface displacements caused by induced tremors. *Applied Sciences* (Switzerland), 10(21), 7660. https://doi.org/10.3390/app10217660.

Pasquali P., Cantone A., Riccardi P., De Filippi M., Ogushi F., Tamura M. & Gagliano S., 2015. Monitoring land subsidence in the Tokyo region with SAR interferometric stacking techniques. [in:] Margottini C., Alcañiz J.M. & López Jiménez J.A. (eds.), *Engineering Geology for Society and Territory – Volume 5: Urban Geology, Sustainable Planning and Landscape Exploitation*, Springer, Berlin, Heidelberg, 995–999. https://doi.org/10.1007/978-3-319-09048-1_191.

Peng S.S., 1986. *Coal Mine Ground Control*. John Wiley & Sons, New York.

Perski Z., 1998. Applicability of ERS-1 and ERS-2 InSAR for land subsidence monitoring in the Silesian coal mining region, Poland. *International Archives of Photogrammetry and Remote Sensing*, 32(7), 555–558.

Przyłucka M., Perski Z. & Kowalski Z., 2024. Long-term subsidence over the Upper Silesia Coal Basin identified on differential LIDAR (2012–2021) and InSAR (2015–2020) data. *Geological Quarterly*, 68(2), 17. https://doi.org/10.7306/gq.1745.

Sandwell D., Mellors R., Tong X., Wei M. & Wessel P., 2011. Open radar interferometry software for mapping surface deformation. *Eos, Transactions American Geophysical Union*, 92(28), 234. https://doi.org/10.1029/2011EO280002.

Shen B., King A. & Guo H., 2008. Displacement, stress and seismicity in roadway roofs during mining-induced failure. *International Journal of Rock Mechanics and Mining Sciences*, 45(5), 672–688. https://doi.org/10.1016/j.ijrmms.2007.08.011.

Tajduś K., 2015. Analysis of horizontal displacement distribution caused by single advancing longwall panel excavation. *Journal of Rock Mechanics and Geotechnical Engineering,* 7(4), 395–403. https://doi.org/10.1016/j.jrmge.2015.03.012.

Tang F., Dong L., Wang Z. & Huang J., 2019. A 3-D inversion model for InSAR detected displacements based on ground subsidence symmetry induced by horizontal coal mining. *Journal of China Coal Society*, 44(1), 210–220. https://doi.org/10.13225/j.cnki.jccs.2018.0698.

Wang Y.Q., Wang Z.F. & Cheng W.C., 2019. A review on land subsidence caused by groundwater withdrawal in Xi'an, China. *Bulletin of Engineering Geology and the Environment*, 78(4), 2851–2863. https://doi.org/10.1007/s10064-018-1278-6.

Wang Y., Yang Z., Li Z., Zhu J. & Wu L., 2020. Fusing adjacent-track InSAR datasets to densify the temporal resolution of time-series 3-D displacement estimation over mining areas with a prior deformation model and a generalized weighting least-squares method. *Journal of Geodesy*, 94(5), 47. https://doi.org/10.1007/s00190-020-01374-8.

Witkowski W.T., Mrocheń D., Sopata P. & Stoch T., 2021. Integration of the leveling observations and PSInSAR results for monitoring deformations caused by underground mining. [in:] *2021 IEEE International Geoscience and Remote Sensing Symposium (IGARSS)*, IEEE, 6614–6617. https://doi.org/10.1109/IGARSS47720.2021.9553988.

Wright T.J., Parsons B.E. & Lu Z., 2004. Toward mapping surface deformation in three dimensions using InSAR. *Geophysical Research Letters*, 31(1), L01607. https://doi.org/10.1029/2003GL018827.

Xie Y., Bagan H., Tan L., Te T., Damdinsuren A. & Wang Q., 2024. Time-series analysis of mining-induced subsidence in the arid region of Mongolia based on SBAS-InSAR. *Remote Sensing*, 16(12), 2166. https://doi.org/10.3390/rs16122166.

Yan S., Liu G., Deng K., Wang Y., Zhang S. & Zhao F., 2016. Large deformation monitoring over a coal mining region using pixel-tracking method with high-resolution Radarsat-2 imagery. *Remote Sensing Letters*, 7(3), 219–228. https://doi.org/10.1080/2150704X.2015.1126683.

Yang Z., Li Z., Zhu J., Wang Y. & Wu L., 2020. Use of SAR/InSAR in mining deformation monitoring, parameter inversion, and forward predictions: A review. *IEEE Geoscience and Remote Sensing Magazine*, 8(1), 71–90. https://doi.org/10.1109/MGRS.2019.2954824.

Yang S., Zhang D., Wang M. & Li J., 2023. Ground and tunnel deformation induced by excavation in pipe-roof preconstruction tunnel: A case study. *Tunnelling and Underground Space Technology*, 131, 104832. https://doi.org/10.1016/j.tust.2022.104832.

Yu C., Li Z., Penna N.T. & Crippa P., 2018. Generic atmospheric correction model for Interferometric Synthetic Aperture Radar observations. *Journal of Geophysical Research: Solid Earth*, 123(10), 9202–9222. https://doi.org/10.1029/2017JB015305.

Zhao H., Ma F. & Zhang Y., 2013. Monitoring and analysis of the mining-induced ground movement in the Longshou Mine, China. *Rock Mechanics and Rock Engineering*, 46(1), 207–211. https://doi.org/10.1007/s00603-012-0232-3.